# Impacts of Cloud Droplet–Nucleating Aerosols on Shallow Tropical Convection

STEPHEN M. SALEEBY, STEPHEN R. HERBENER, AND SUSAN C. VAN DEN HEEVER

*Colorado State University, Fort Collins, Colorado*

TRISTAN L'ECUYER

*University of Wisconsin–Madison, Madison, Wisconsin*

(Manuscript received 27 May 2014, in final form 22 December 2014)

ABSTRACT

Low-level warm-phase clouds cover a substantial portion of Earth's oceans and play an important role in the global water and energy budgets. The characteristics of these clouds are controlled by the large-scale environment, boundary layer conditions, and cloud microphysics. Variability in the concentration of aerosols can alter cloud microphysical and precipitation processes that subsequently impact the system dynamics and thermodynamics and thereby create aerosol–cloud dynamic–thermodynamic feedback effects. In this study, three distinct cloud regimes were simulated, including stratocumulus, low-level cumulus (cumulus under stratocumulus), and deeper cumulus clouds. The simulations were conducted without environmental large-scale forcing, thereby allowing all three cloud types to freely interact with the environmental state in an undamped fashion. Increases in aerosol concentration in these unforced, warm-phase, tropical cloud simulations lead to the production of fewer low-level cumuli; thinning and erosion of the widespread stratocumulus layer; and the development of deeper, inversion-penetrating cumuli. The mechanisms for these changes are explored. Despite the development of deeper, more heavily precipitating cumuli, the reduction of the widespread moderately precipitating stratocumulus clouds leads to an overall reduction in domainwide accumulated precipitation when aerosol concentrations are enhanced.

## 1. Introduction

Shallow marine clouds are the most prolific cloud type on Earth as determined from *CloudSat* data (Sassen and Wang 2008), surface observations (Hahn and Warren 2007), and the International Satellite Cloud Climatology Project (Rossow and Schiffer 1999). They cover nearly 20%–25% of Earth's surface area (Turner et al. 2007; Wood 2012) and are highly important to the global water and energy budgets (Hartmann et al. 1992). Shallow, low-level cumuli cover much of the tropical oceans and are often found beneath widespread, inversion-topped stratocumulus clouds where they act to feed heat and moisture to the stratocumulus layer, thereby sustaining it (Augstein et al. 1973; Stevens et al. 2001; Xue et al. 2008). Isolated areas of greater instability beneath stratocumulus clouds can be generated by precipitation–evaporation processes and permit the formation of deep trade cumuli that penetrate through the inversion layer (Paluch and Lenschow 1991; Stevens et al. 1998). Further, cold-pool outflow generated from the evaporation of precipitation can induce zones of convergence that assist in the generation of new cumuli (Xue et al. 2008). These three low-level cloud regimes (shallow cumulus, stratocumulus, and deeper cumulus clouds) ultimately act to moisten the boundary layer in support of subsequent tropospheric deep convection that aids in establishing the heat and moisture balance (Riehl and Malkus 1957; Augstein et al. 1973; Hartmann et al. 1992). As such, understanding the processes that impact the cloud fraction and relative distribution of these warm-phase low-level cloud regimes is of great importance.

Hygroscopic aerosols are one such phenomenon known to impact cloud characteristics and precipitation processes (Albrecht 1989). Aerosol-induced perturbations to shallow tropical clouds have potentially significant global impacts that are still poorly understood (Solomon et al. 2007). Both satellite studies (Sekiguchi et al. 2003; Matsui et al. 2004; Koren et al. 2005;

*Corresponding author address:* Stephen Saleeby, Atmospheric Science Department, Colorado State University, 1371 Campus Delivery, Fort Collins, CO 80526.
E-mail: smsaleeb@atmos.colostate.edu

DOI: 10.1175/JAS-D-14-0153.1

Kaufman et al. 2005; Berg et al. 2006, 2008) and numerical modeling studies (Feingold et al. 1996; Stevens et al. 1998; Jiang et al. 2002; Jiang and Feingold 2006; Ackerman et al. 2004; Xue and Feingold 2006; Xue et al. 2008; Savic-Jovcic and Stevens 2008; Lee et al. 2009) of tropical stratocumulus and shallow cumulus clouds have sought to determine how such clouds will respond to changes in aerosol concentration. For example, cloud liquid water path (LWP) has been found to be a function of cloud thickness (Lee et al. 2009), cloud fraction and type (Jiang and Feingold 2006), precipitation rate (Ackerman et al. 2004; Xue et al. 2008), relative humidity above the trade inversion (Ackerman et al. 2004; Lee et al. 2009), and the strength of large-scale subsidence (Jiang et al. 2002). Because of complex feedbacks that exist among aerosols, cloud microphysics, dynamics, and thermodynamics, the aerosol–cloud–precipitation relationship appears to vary substantially among cloud types (Seifert and Beheng 2006; Khain et al. 2008; van den Heever et al. 2011).

Previous modeling studies of shallow tropical clouds have addressed aerosol effects within constrained environments that tend to force the environment toward the initial conditions (e.g., Stevens et al. 2001; Cheng et al. 2009; Xue et al. 2008; Lee et al. 2009). While this is necessary to maintain a specific simulated cloud field, it imposes a limit on the aerosol impacts by dampening the aerosol–cloud dynamic–thermodynamic feedbacks. Jiang et al. (2002) demonstrated that greater magnitude cloud impacts and dynamic feedbacks within a stratocumulus environment occur in response to aerosol loading as the large-scale subsidence is reduced. Waite and Khouider (2010) simulated multiple clouds regimes from shallow cumuli to deeper convection by withholding large-scale forcing and allowing the model to evolve more freely.

This manuscript presents results from a numerical modeling study that is based on the Atlantic Trade Wind Experiment (ATEX) (Augstein et al. 1973, 1974; Brümmer et al. 1974). ATEX has formed the basis of previous studies of trade wind boundary layer clouds (e.g., Albrecht 1979; Stevens et al. 2001; Xue et al. 2008). In the study presented herein, simulations were performed to investigate the range of aerosol effects on warm-phase tropical clouds simulated in an environment in which large-scale forcings were omitted, thereby allowing aerosol–cloud dynamic–thermodynamic interactions and feedbacks to occur without artificially damping such processes. Furthermore, the lack of large-scale forcing permits for the simultaneous occurrence of the low-level cumulus, stratocumulus, and deeper cumulus clouds, and the examination of aerosol impacts on all three clouds regimes, which is of specific interest to this study.

In these simulations, aerosols act as the catalyst to promote changes in the cloud droplet distribution that then impact the environment through heating and cooling related to condensation and evaporation. The environmental response to changes in microphysical processes is manifested through changes in vertical motion, precipitation, cold pools, and surface convergence that then feed back to the cloud and thermodynamic state. By permitting undamped model feedbacks, these simulations represent what could be considered to be the upper limit of aerosol indirect effects within these three warm-phase cloud regimes.

This study was performed to seek answers to the following questions: 1) Can aerosols induce warm-phase convective invigoration that would lead to deeper-penetrating cumuli? 2) How does an increase in aerosol concentration alter the cloud regimes and cloud dynamic–thermodynamic feedbacks? 3) What is the response in the precipitation and distributions of cloud liquid water path and rainfall rate? These questions will be addressed by examining aerosol–cloud dynamic–thermodynamic characteristics and interactions related to fundamental microphysical and dynamical processes.

## 2. Model and experiment description

### a. *Model description*

The Colorado State University Regional Atmospheric Modeling System (RAMS) (Cotton et al. 2003), version 6.0, was run as a 3D cloud-resolving model (CRM). The model domain was 100 km × 100 km × 4 km with uniform 250-m horizontal and 100-m vertical grid spacings. The top four layers were Rayleigh absorbing layers. Simulations were run with doubly periodic boundary conditions in the horizontal, the Smagorinsky (1963) turbulent diffusion scheme, a two-stream, hydrometeor-sensitive, radiation scheme (Harrington 1997), the LEAF surface flux model (Walko et al. 2000b), and two-moment microphysics (Meyers et al. 1997; Saleeby and Cotton 2004; Saleeby and van den Heever 2013).

The microphysics model prognoses mass mixing ratio and number concentration of cloud and drizzle droplets, rain, pristine ice, snow, aggregates, graupel, and hail. In this study the simulated clouds remain below the freezing level, and thus, ice particles are absent. Aerosol activation/cloud droplet nucleation is simulated according to Saleeby and Cotton (2004) and Saleeby and van den Heever (2013), whereby a population of aerosols may act as cloud condensation nuclei (CCN) depending on environmental temperature, vertical velocity, aerosol concentration, and aerosol size. Autoconversion of cloud droplets to drizzle and rain, as well as accretion processes, are simulated in a bin-emulating sense [Tzivion (Tzitzvashvili) et al. 1987] using size-dependent collection kernels. Vapor and

heat diffusion of hydrometeors is parameterized according to Walko et al. (2000a), and sedimentation is represented in a bin-emulating manner (Feingold et al. 1998). Given the warm nature of these clouds, droplet nucleation, collision–coalescence, condensation–evaporation, and sedimentation are the only active microphysical processes.

### b. Initialization, experiments, and analyses

Numerical simulations were initialized horizontally homogeneously with a composite average atmospheric sounding from ATEX and a constant observed sea surface temperature of 298 K (Stevens et al. 2001) and were run for 36 h. Small, randomized, near-surface potential temperature perturbations were applied on the first time step to break the initial model horizontal homogeneity. Simulations were initialized with varying concentrations of submicron (median radius of 0.04 $\mu$m) aerosols. For simplicity, these aerosols will be referred to as CCN. The notation for the number concentrations will be designated via bounding brackets as [CCN]. The sensitivity simulations were initialized with aerosol profiles that decreased linearly with height from the surface to the model top (4 km). The CCN sensitivity tests were initialized with maximum surface concentrations of 50, 100, 200, 400, 800, and 1600 cm$^{-3}$. Varying [CCN] from the time of model initialization was done to include the aerosol effects on all phases of the cloud life cycles.

Given the duration of the simulations, the use of periodic boundary conditions, and the lack of external aerosol emission sources in these simulations, aerosol sinks were not permitted. Aerosols were allowed to undergo mixing and transport throughout the model domain. This aerosol treatment is a proxy for continuous large-scale transport of aerosols that maintain local concentrations in the domain. During the cloud droplet nucleation process, aerosols are activated and droplets are nucleated with respect to the amount of available supersaturation and predicted fraction of activated aerosols. Under these conditions, nucleation of additional droplets only occurs if the number of predicted activated aerosols exceeds the current cloud droplet number concentration. This method prevents overnucleation in the absence of explicit aerosol sources and sinks.

In these simulations, the first 12 h are considered as the model spinup and cloud development period. In the final 24 h, the three cloud regimes of interest are evident, and thus, this time period of the simulations is analyzed. Our intent is to examine the aerosol-induced differences in the different cloud types, microphysical processes, and dynamic feedbacks. This is achieved primarily through temporal and spatial averaging of the model output, which allows for a more objective identification of the strongest aerosol-induced signals.

Throughout the analyses that follow, multiple cloud regimes and layers will be discussed, and thus, it helps to establish some common terminology to refer to these cloud regimes. The combination of low-level cumulus and stratocumulus clouds is frequently addressed as ''cumulus under stratocumulus,'' but distinct terminology for each cloud regime will be used for clarity in the following discussion. The cloud-layer naming convention that follows is based on the vertical profiles of cloud properties (evident in Figs. 5 and 6): 1) the subcloud layer exists below 800 m, 2) low-level cumulus clouds exist from 800 to 1300 m, 3) stratocumulus clouds exist from 1300 to 2200 m, and 4) deep cumulus clouds exist above 2200 m. Layers 1–3 are closely comparable to those highlighted by Xue et al. (2008). The cloud-layer definitions vary slightly among experiments as the cloud heights vary with [CCN].

## 3. Results of CCN experiments

Figure 1 offers a visual perspective of the cloud field being simulated in this study under varying aerosol conditions. Much of the domain is covered with stratocumulus clouds at the beginning and end of the analysis period for both clean and polluted simulations, and the fields are interspersed with areas of higher LWP that would tend to indicate deeper clouds. At the beginning of the analysis period the clean and polluted simulations have already begun to diverge with respect to the cloud field distribution. By the end of the analysis period in both simulations there is noticeably less cloud coverage with less LWP and embedded areas with increased LWP. While Fig. 1 displays only single snapshots in time, this comparison of cloud fields at the beginning and end of the analysis period for a single [CCN] suggests that cloud dynamic feedbacks may be inducing erosion of the stratiform layer and development of deeper cumuli. Variations in [CCN] may be modifying the feedback processes that generate the differences in cloud fields seen in a comparison between clean and polluted conditions. The analyses that follow will examine variability in cloud characteristics and dynamical and thermodynamical feedbacks that occur with changes in [CCN] and will offer evidence to explain the physical mechanisms that lead to aerosol-induced variability in cloud fields and precipitation.

### a. Time series of hydrometeor properties

Figure 2 displays time series plots of the spatially averaged mixing ratio, number concentration, and mean diameter of cloud droplets and raindrops with varying

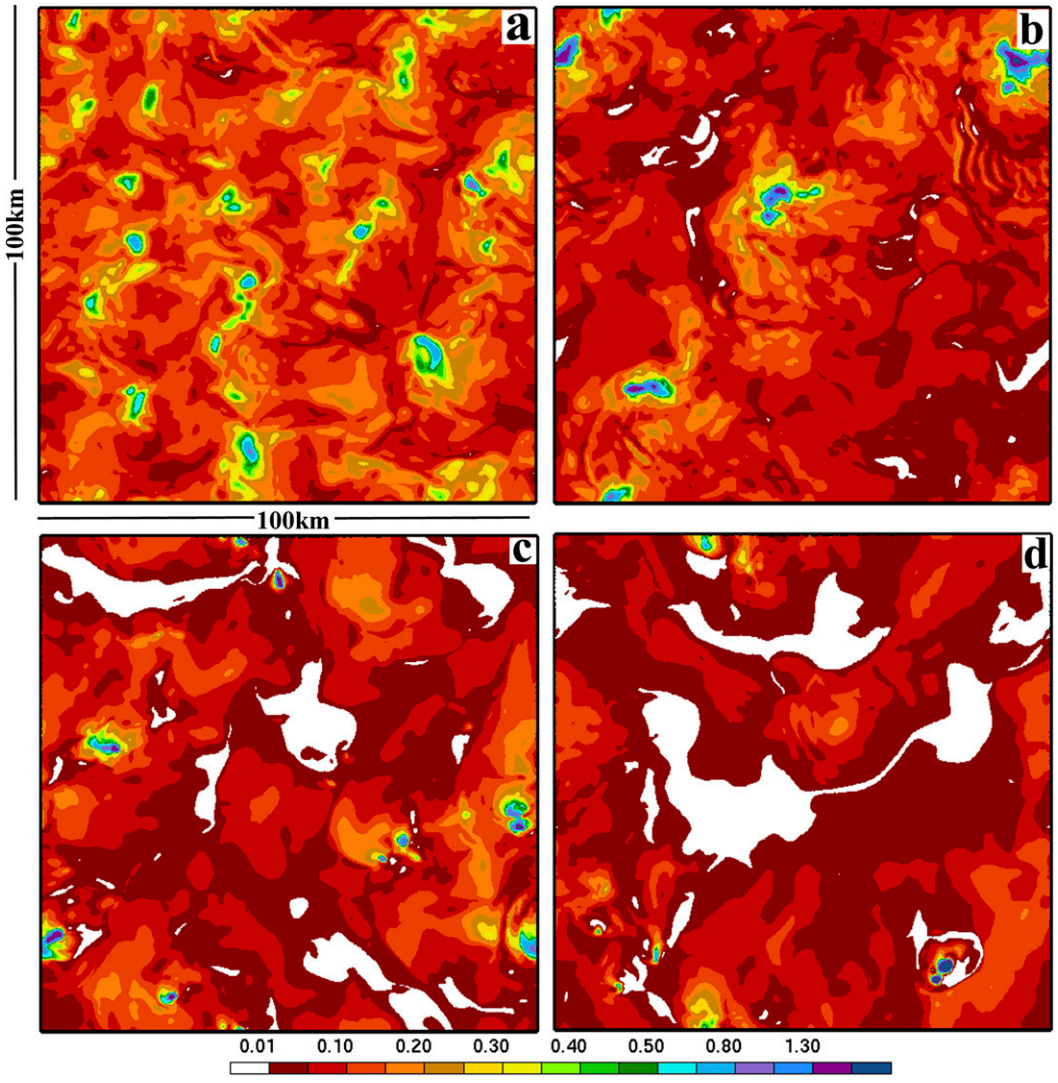


FIG. 1. Representative plan view plots of LWP (mm) from the (a),(b) cleanest and (c),(d) most polluted simulations at the (a),(c) beginning and (b),(d) end of the analysis period.

[CCN]. There is a consistent and nearly monotonic trend in all three properties of the cloud water field. As [CCN] is increased, the cloud droplet mixing ratio increases, number concentration increases, and mean diameter decreases. This aerosol-induced response in the cloud water field generally follows the hypothesis of Twomey (1974, 1977). While the time series trends in rain mixing ratio are less discernable and vary over time, there is a tendency toward an increase in rain mixing ratio in response to an increase in [CCN]. Furthermore, raindrop number concentrations are reduced while mean raindrop diameters are larger. Other studies have also reported a relationship between [CCN] and the production of fewer, but larger raindrops (Altaratz et al. 2008; Berg et al. 2008; Saleeby et al. 2010). This relationship is attributed to a reduction in droplet self-collection due to reduced collection efficiencies among smaller droplets. This slows and reduces the likelihood of the formation of raindrops; however, the raindrops that do form have an abundance of cloud water available for collection as well as less competition for accretion growth, and thus, they tend to grow larger. Though not shown, there is also a monotonic redistribution of total liquid water from rainwater to cloud water as [CCN] is increased. These tendencies are indicative of an aerosol-induced suppression of the warm-rain formation process.

### *b. Liquid water path, rainfall rates, and cloud fraction*

To investigate the aerosol-induced variability in cloud distribution and cloud thickness, the relative frequency of occurrence of clouds over a range of LWP bins for all [CCN] simulations was computed (Fig. 3a). Throughout

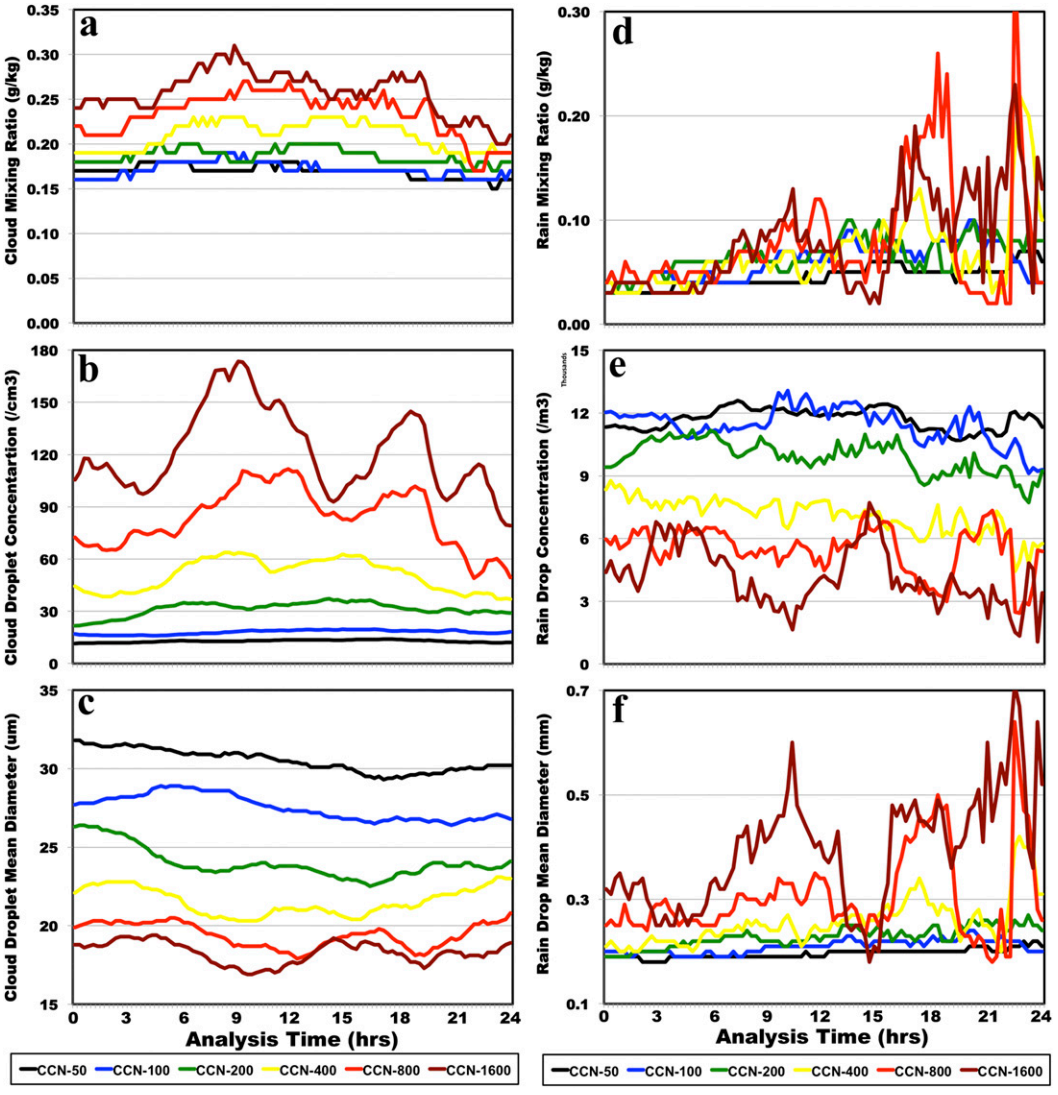


FIG. 2. Time series of domain-averaged (a) cloud mixing ratio (g kg$^{-1}$), (b) cloud droplet number concentration (cm$^{-3}$), (c) cloud droplet mean diameter ($\mu$m), (d) rain mixing ratio (g kg$^{-1}$), (e) raindrop number concentration (m$^{-3}$ $\times$ 1000), and (f) raindrop mean diameter (mm). Grid cells were included in the averages if the respective cloud or rain mixing ratios exceeded 0.01 g kg$^{-1}$. The color scheme in the legend representing the simulations with varying [CCN] is displayed and is utilized in the remainder of the figures.

the analysis and for ease of discussion, LWP (vertically integrated liquid condensate) is used as a metric for cloud thickness; low LWP will be referred to as thin or shallow clouds and high LWP will be referred to as thick or deeper clouds. Calculations of the temporally and spatially averaged LWP of cloudy columns from the simulations with varying [CCN] range approximately from 0.08 to 0.14 mm (80–140 g m$^{-2}$), which is consistent with the range of LWP from the ATEX simulations of Xue et al. (2008).

From Fig. 3a, the cleanest simulation offers its greatest relative contribution to the sum-total cloud frequency within the 0.2–0.3-mm LWP bin with decreasing contributions on either side of this bin. The least contribution in the 0.2–0.3-mm LWP bin comes from the most polluted simulations. The cleanest environment contains no cloudy columns with LWP $>$ 3 mm, while the more polluted scenarios contain some high LWP clouds. As [CCN] increases, there is a shift from clouds with predominantly moderate LWP (0.1–0.9 mm) toward a greater propensity for a combination of both thicker (LWP $>$ 1 mm) and thinner (LWP $<$ 0.09 mm) clouds.

A companion plot in Fig. 3b reveals a similar trend in rainfall rate. The cleanest simulation contributes more than 30% to the ensemble total area of surface rainfall

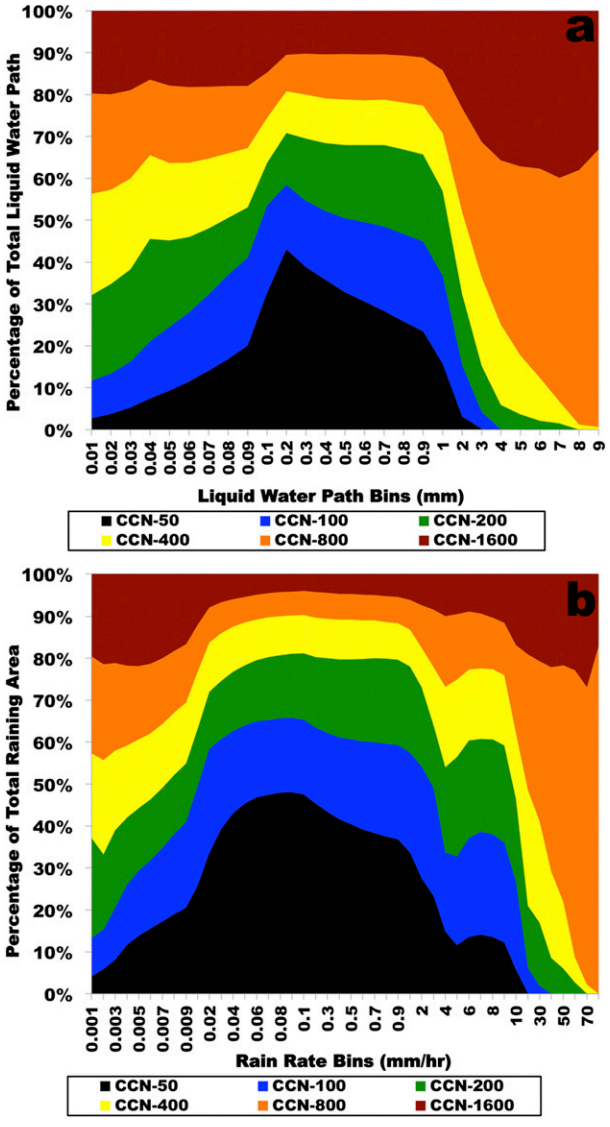


FIG. 3. Percentage contributions, within discrete bins, of (a) LWP and (b) surface rainfall rate. Percentage values are relative to the ensemble total of simulations with [CCN] varying from 50 to 1600 $cm^{-3}$. For example, in (b), CCN-50 contains ~45% of the ensemble total raining grid boxes that have a surface rain rate of 0.08 mm $h^{-1}$.

with rain rates between approximately 0.01 and 2.0 mm $h^{-1}$. At the lightest and heaviest rain rates, the more polluted simulations contribute a greater percentage to the ensemble total. These trends demonstrate that the addition of pollution aerosols induces a change from a field of clouds with a single dominant mode of moderate LWP and rain rates to a more disparate cloud field comprised of relatively low and high LWP and rain rates.

Here, the moderate-LWP clouds are associated with the widespread stratocumulus layer and moderate rainfall rates. Previous studies have shown that the aerosol effect on LWP of stratocumulus clouds is determined by the sum of 1) decreased LWP from enhanced entrainment–evaporation effects and 2) increased LWP by suppression of precipitation (Ackerman et al. 2004; Jiang and Feingold 2006). The environment in this study is characterized by dry air above the inversion, which tends to allow the decrease in stratocumulus LWP from entrainment to prevail over the impacts of precipitation suppression (Ackerman et al. 2004; Lee et al. 2009).

The change in the cloud-type distribution toward an increased frequency of both shallower and deeper clouds, following an increase in [CCN], has a profound effect on accumulated rainfall. Figure 4a shows that the accumulated rainfall volume decreases by over 50% between simulations with the lowest and highest [CCN]. This figure indicates that the moderate rain rates (around 0.01 mm $h^{-1}$) contribute most readily to rain volume in the cleanest environments. Figure 4b presents accumulated surface rain rate by bin, which is a proxy for accumulated rain volume per rain-rate bin. As the frequency of occurrence of the moderate rain rates is reduced for higher [CCN], the total rainfall volume begins to decline. At higher [CCN], the lightest rain rates contribute more significantly to the total rainfall volume. While the lightest rain rates also occur more frequently (Fig. 4c), they cannot produce the same total rain volume as the moderate rain rates, and thus, the total water reaching the surface decreases with increasing [CCN]. Though convective rain rates are quite large and occur more frequently in the more polluted simulations (Fig. 3b), they are fewer in number (Fig. 4c), and thus, their contribution to total rainfall is quite small.

The vertical profiles of cloud and rain fractions (Fig. 5) are quite comparable to those demonstrated in Stevens et al. (2001) and Xue et al. (2008). As [CCN] is increased, the total cloud volume, as represented by the area under the curves (Fig. 5a), decreases, the maximum horizontal cloudy area decreases, the predominant height of occurrence increases, and the primary cloud-base height increases. This reveals an aerosol-induced reduction in cloud area, increase in cloud-top and cloud-base heights, and reduced cloud thickness. The reduction in the fraction of low-level cumulus clouds with increasing [CCN] is attributed to weaker subcloud conditional instability that occurs from suppressed precipitation and less rain evaporation (Paluch and Lenschow 1991; Stevens et al. 1998) and reduced surface convergence resulting from weaker cold pools (Fig. 8). Xue et al. (2008, their Fig. 3a) also found a decrease in both cloud fraction and low-level cumuli following an increase in [CCN]; however, they did not encounter an increase in cloud-top height. The difference in the cloud-top height can be attributed to the fact that large-scale subsidence is not

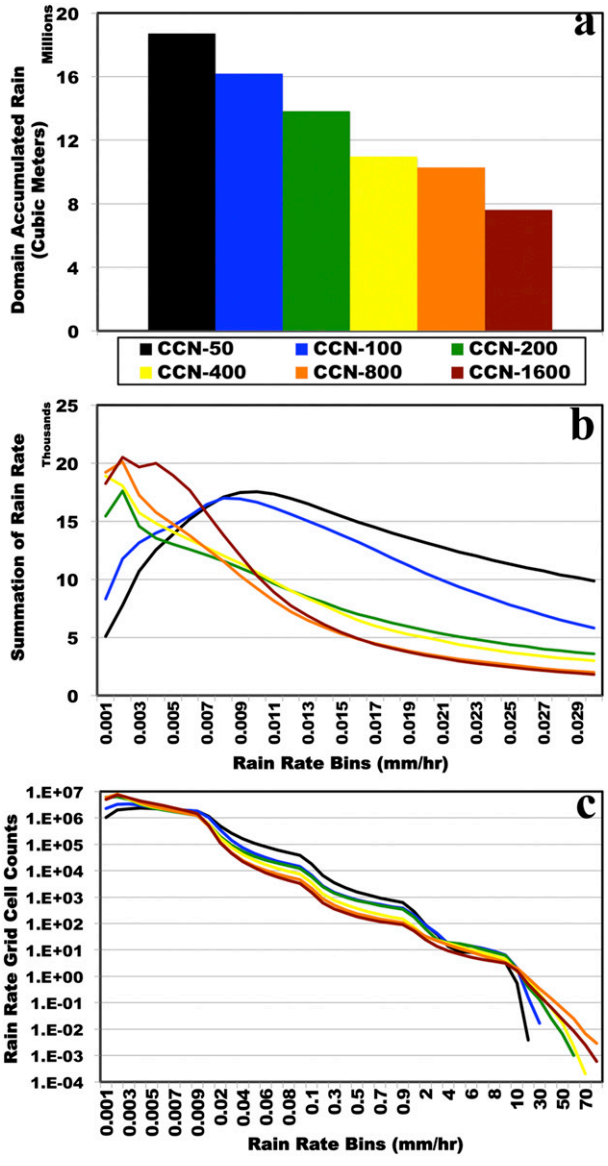


FIG. 4. (a) Domain-summed surface accumulated rainwater volume ($m^3$), (b) simulation-summed surface rain rate (mm) within discrete bins, and (c) surface rain-rate grid cell counts normalized within discrete bins.

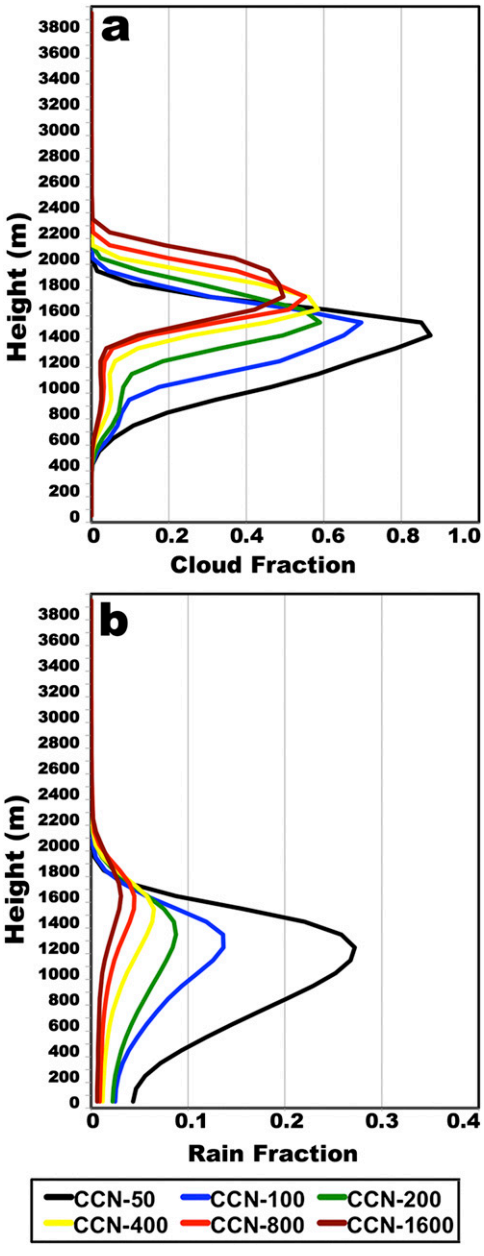


FIG. 5. Temporally and spatially averaged vertical profiles of (a) cloud fraction and (b) rain fraction. Grid cells were included in the averages if the respective cloud or rain mixing ratios exceeded 0.01 g $kg^{-1}$.

imposed in our simulations as discussed earlier (Jiang et al. 2002), and as such, growth of clouds by invigoration and deepening of the boundary layer is permitted (see Fig. 10). Similar trends exist in the rain area fraction (Fig. 5b) as well. These processes will be discussed in detail in subsequent sections. In the following discussion of cloud- and rain-area-averaged vertical profiles, it is useful to keep in mind that the cloud-fraction profiles (Figs. 5a,b) impact the interpretation of the variability and magnitude at various altitudes within the profiles since the fraction of cloud and rain area, and thus number of sampled grid cells, varies considerably with height.

### c. *Vertical distribution of cloud and rain properties*

There is a consistent increase in the average cloud-top height and average cloud mixing ratio of the deep cumuli for an increase in [CCN] (Fig. 6a). In the low-level cumulus and stratocumulus layers there is a general trend toward greater cloud mixing ratio for greater

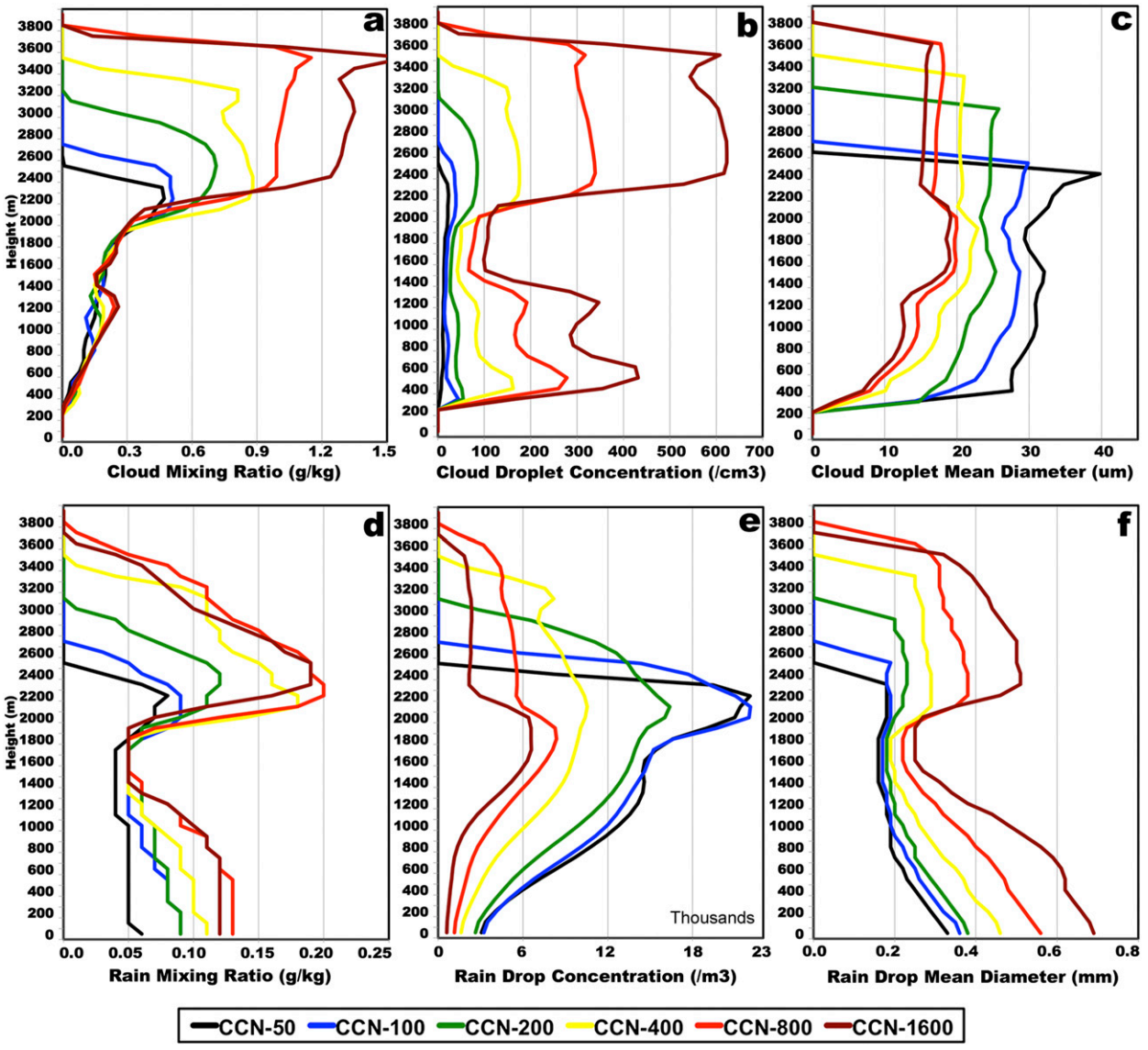


FIG. 6. Temporally and spatially averaged vertical profiles of (a) cloud droplet mixing ratio ($g\,kg^{-1}$), (b) cloud droplet number concentration ($cm^{-3}$), (c) cloud droplet mean diameter ($\mu m$), (d) rain mixing ratio ($g\,kg^{-1}$), (e) raindrop number concentration ($m^{-3} \times 1000$), and (f) raindrop mean diameter (mm). Grid cells were included in the averages if the respective cloud or rain mixing ratios exceeded $0.01\,g\,kg^{-1}$.

[CCN], though this varies with height. Note that in the simulations with the greatest [CCN] the maximum cloud-top heights approach the model top and are thus limited from additional growth. The model lid and absorbing layer act to prevent formation of congestus and deep convection and allow us to keep our cloud analysis within a simplified warm-rain regime. However, over the duration of these simulations the clouds that approach the model top are relatively few.

Similar to the time series of rain properties, the vertical rain distributions (Figs. 6d–f) are affected by the aerosol-induced changes in the cloud properties such that the average rain mixing ratio generally increases, raindrop number concentration decreases, and raindrop mean diameter increases. The raindrop number concentration and mean diameter trends are consistent with height and reveal a reduction in conversion from cloud to rainwater. The presence of greater average rain mixing ratio does not contradict the warm-rain suppression effect of aerosols, but rather, is indicative of development of deeper clouds with greater total water.

The averaged cloud and rain profiles become even more interesting when considered within the context of the cloud fraction (Fig. 5a). Recall that the greatest

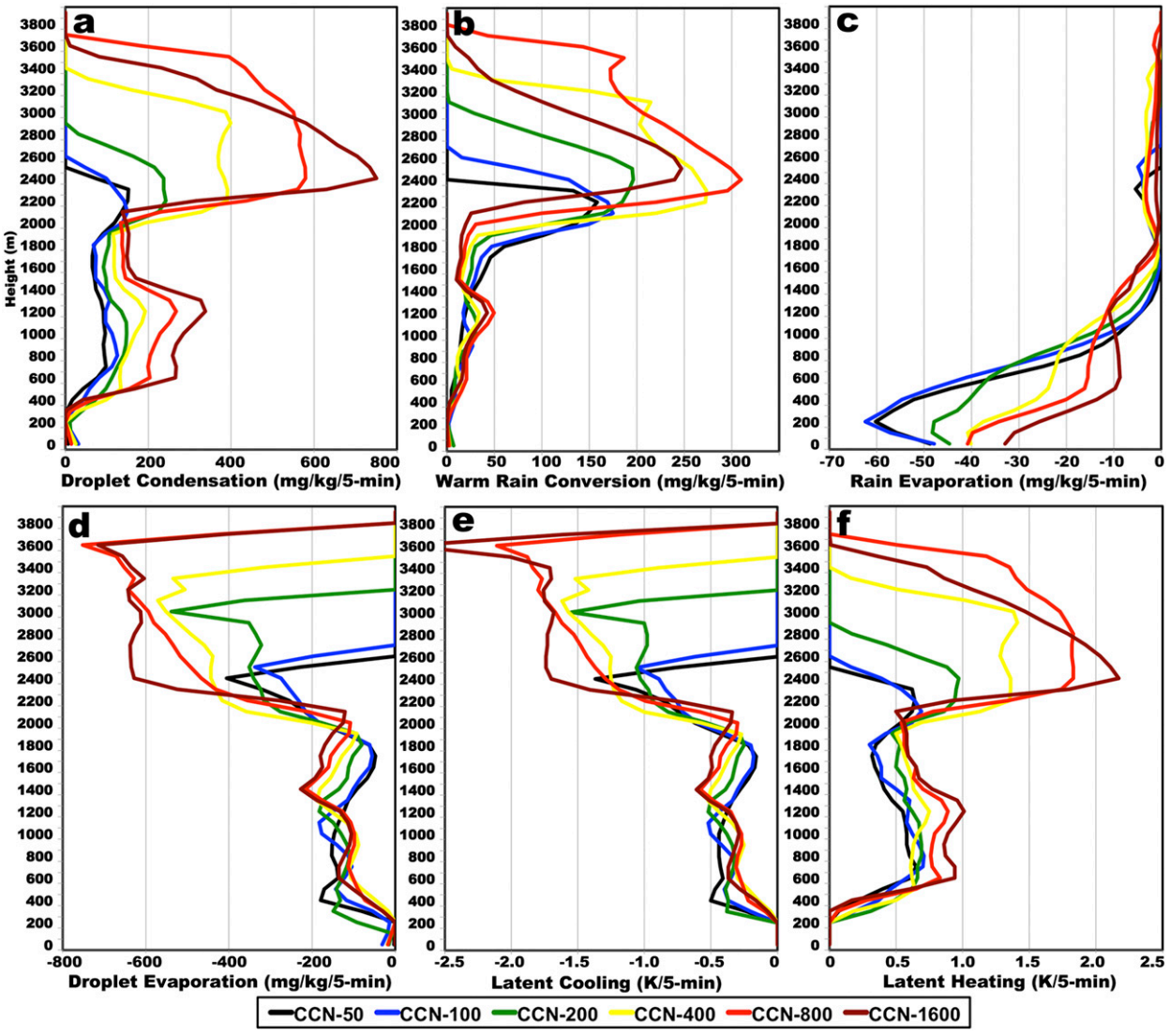


FIG. 7. Temporally and spatially averaged vertical profiles of the microphysical processes [mg kg$^{-1}$ (5 min)$^{-1}$] of (a) cloud droplet condensation growth, (b) cloud and drizzle droplet to raindrop conversion by autoconversion and accretion, (c) raindrop evaporation, and (d) cloud droplet evaporation, and in-cloud heating profiles [K (5 min)$^{-1}$] of (e) latent cooling and (f) latent heating. Grid cells were included in the averages if the respective cloud or rain mixing ratios exceeded 0.01 g kg$^{-1}$ and microphysical budget values were nonzero.

cloud fraction occurs within the stratocumulus layer. This layer corresponds to the relative minimum in average cloud drop number concentration (Fig. 6b), rain mixing ratio (Fig. 6d), and raindrop diameter (Fig. 6f). These relative minima result from the averaging of dynamically weak stratocumulus clouds in this layer. The greater average cloud droplet concentration above and below the stratocumulus layer is indicative of predominantly cumuliform clouds with stronger vertical motion (Fig. 9b). Stronger updrafts in these layers lead to greater supersaturation, which increases droplet nucleation, droplet concentrations, and condensation growth (Fig. 7a). These dynamical differences in the cloud layers impact the distinct microphysical differences in hydrometeor characteristics.

The change in raindrop concentration and mean diameter in the subcloud layer is a consequence of rain evaporation. The population of more numerous but smaller raindrops that exists in the cleanest simulations is more susceptible to evaporative processes; as such, the raindrop concentration reduces more dramatically by evaporation in the cleaner cases (Fig. 6e). As the smallest raindrops evaporate in the more polluted cases, the larger drops that are less susceptible to evaporation remain, which results in an increase in mean raindrop diameter as drops fall to the surface (Fig. 6f). Similar responses in rain

evaporation due to aerosol loading have been reported in previous studies (Altaratz et al. 2008; Berg et al. 2008; Saleeby et al. 2010; Storer et al. 2010; van den Heever et al. 2011; Storer and van den Heever 2013).

### d. Microphysical processes and cold pool diagnostics

Thus far, the microphysical pathways that lead to changes in cloud water, rainwater, and precipitation have been speculated. In Fig. 7 the vertical profiles of the primary microphysical processes that contribute to condensate distributions are compared. These include condensation growth of cloud droplets, conversion of cloud to rainwater, and raindrop evaporation. Condensation growth of cloud droplets (Fig. 7a) is a necessary mechanism for the growth of droplets to the critical size needed to initiate droplet autoconversion and accretion. Figure 7a shows that as [CCN] is increased, there is an increase in the average condensational growth over the depth of the clouds. In the more polluted scenarios there are more numerous droplets, and therefore, a greater net surface area is available for the deposition of vapor (e.g., Saleeby et al. 2010; Storer and van den Heever 2013). The greater condensation projects directly onto the profiles of latent heating (Fig. 7f), which reveal a trend of increased average latent heat release over the cloud depth as [CCN] increases. Enhanced condensation and latent heating will tend to increase positive buoyancy, which has implications for vertical motion and is discussed in the following section. Despite the greater net condensation in polluted scenarios, the mean droplet size remains smaller (Fig. 6c), since vapor condensation is spread over an increased droplet population and would, therefore, tend to have lower collection efficiencies.

The trend in droplet growth through collision–coalescence varies with height as [CCN] is increased (Fig. 7b). If the variable height of the stratocumulus layer is visually adjusted among aerosol simulations to a common altitude, then the following observations can be made. There is a monotonic decrease in the conversion of cloud to rainwater, indicative of warm-rain suppression. Above this layer there is a large increase in the average conversion of cloud to rainwater for an increase in [CCN] in association with deeper cumuli and greater average cloud water (see Fig. 6a).

It has been demonstrated that as [CCN] is increased, the raindrop spectra contain fewer, but larger, drops (Figs. 2e,f and 6e,f). This has a direct influence on raindrop evaporation. In the average profile of rain evaporation (Fig. 7c) there is a trend in the subcloud layer toward reduced rain evaporation with increasing [CCN]. This process is responsible for the presence of greater rain mixing ratio near the surface (Fig. 6d) as well as for the differences in the slopes of the vertical profiles of rain number concentration (Fig. 6e) and mean diameter (Fig. 6f) between the cleanest and most polluted simulations (e.g., Saleeby et al. 2010).

The profiles of average cloud droplet evaporation (Fig. 7d) reveal a distinct trend toward greater evaporation in the stratiform and cumuliform layers for greater [CCN]. A population of more numerous, smaller droplets in higher [CCN] environments is more susceptible to evaporation owing to an increased surface area to volume ratio (e.g., Saleeby et al. 2010; Storer and van den Heever 2013). As expected, the profiles and trends of latent cooling (Fig. 7e) look very similar to cloud evaporation since cloud droplet evaporative cooling is the primary process contributing to latent cooling. In areas of entrainment near cloud top, an increase in evaporation will tend to induce an increasing positive entrainment–evaporation feedback process. Horizontal variability in evaporation tends to generate horizontal temperature gradients through evaporative (latent) cooling, which generates buoyancy gradients that further fuel mixing and entrainment (Blyth et al. 1988; Zhao and Austin 2005; Xue and Feingold 2006).

The substantial reduction in subcloud rain evaporation with an increase in [CCN], discussed above, has direct implications for cold-pool strength and the subsequent outflow convergence that assists in driving the formation of low-level cumuli that feed and sustain the stratiform layer. Figure 8a reveals that in raining downdrafts near the surface the negative buoyancy generated by evaporative cooling becomes less negative as [CCN] increases and rain evaporation decreases. This effect impacts the cold-pool characteristics. Figures 8b and 8c generally reveal increases in the potential temperature $\Theta$ and the perturbation of potential temperature $\Theta'$ as [CCN] increases from a clean to a more polluted state. These trends in $\Theta$ and $\Theta'$ indicate the presence of warmer cold pools at higher [CCN]. Furthermore, Fig. 8d reveals a monotonic decrease with increasing [CCN] in the fraction of the domain with cold-pool $\Theta'$ depressions stronger than $-0.5\,\mathrm{K}$. The combination of these trends in cold-pool strength and area of influence suggests that the influence of cold-pool outflow should decrease in magnitude and expanse for an increase in [CCN] and, thus, reduce the dynamic response to interacting cold-pool boundaries. Figures 8e and 8f display the mean positive surface convergence and the domain fraction where positive surface convergence is greater than $10^{-4}\,\mathrm{s}^{-1}$. These figures reveal both a reduction in the magnitude of surface convergence as well as the area over which convergence is present. Such reductions lead to less cold-pool forcing to support development of low-level cumuli. Finally,

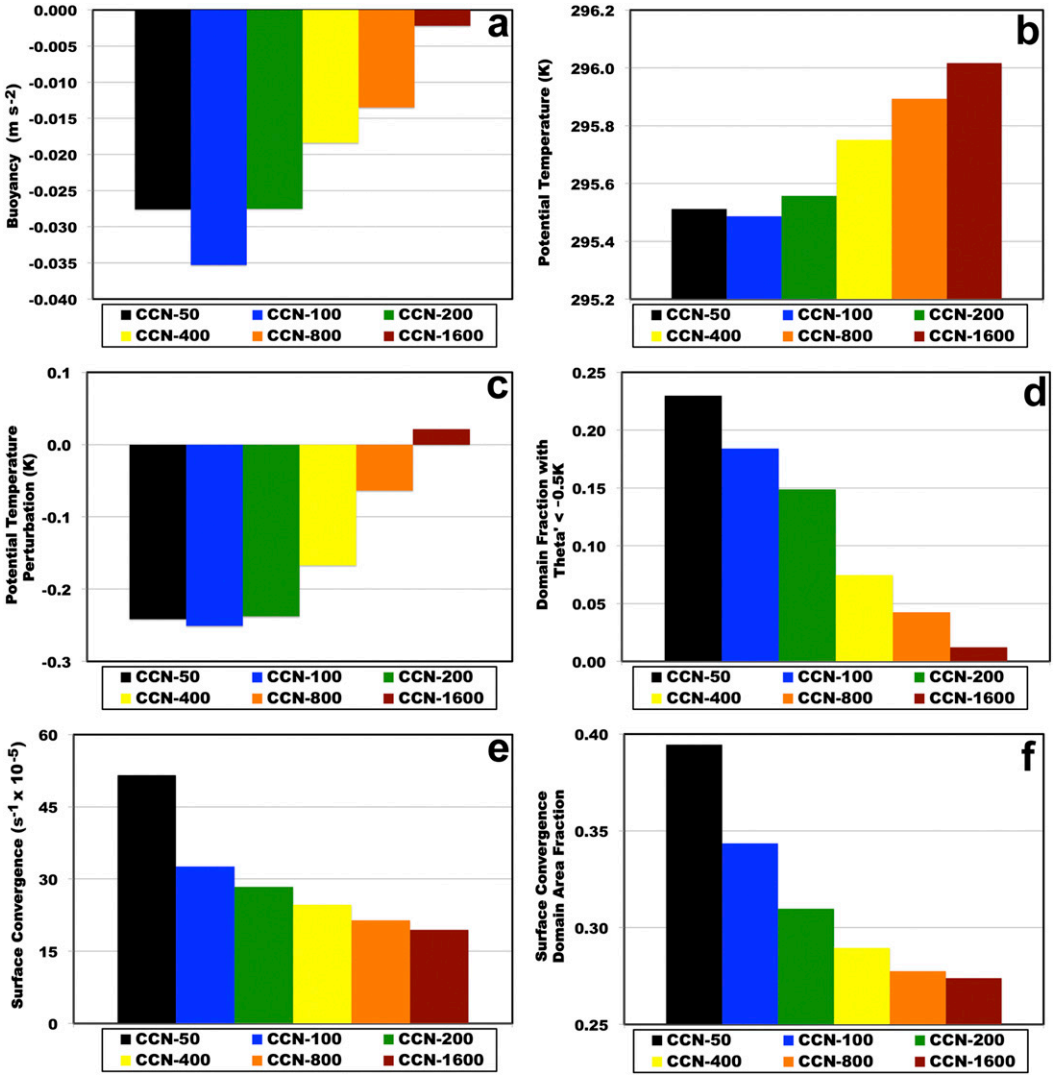


FIG. 8. Histogram of temporally and spatially averaged (a) buoyancy ($m\,s^{-2}$) within raining downdrafts at the lowest model level, (b) $\Theta$ (K), (c) $\Theta'$ (K), (d) domain fraction with $\Theta' < -0.5$ K, (e) surface convergence ($s^{-1} \times 10^5$), and (f) domain fraction with surface convergence greater than $10^{-4}\,s^{-1}$.

upward vertical motion in excess of $10\,cm\,s^{-1}$ at the lowest model levels, where outflow convergence has a direct influence, occurs nearly an order of magnitude less frequently in the most polluted case compared to the cleanest (not shown). These cold-pool effects contribute to the reduction of the low-level cumulus under stratocumulus clouds for an increase in [CCN], as indicated in Fig. 5a.

### e. *Vertical velocity, variance, and skewness*

Figure 9 displays temporally and spatially averaged profiles of vertical velocity as well as its variance and skewness. Over most of the vertical profile there are increases in both domainwide (Fig. 9a) and in-cloud (Fig. 9b) updraft strength with an increase in [CCN]. Within this warm-rain cloud system there is a thermodynamic feedback linking cloud microphysics and vertical velocity whereby condensation growth of cloud droplets (Fig. 7a) releases latent heat, which increases buoyant forcing of the updrafts. In turn, vertical motion lifts an air parcel, which saturates, and allows for further condensation and latent heating. Once an initial updraft forms, the more numerous cloud droplets within polluted conditions allows for more efficient vapor consumption and condensation and further invigoration. Additional condensation also increases condensate drag, which works in opposition to latent heating; however, computations (not shown) revealed these offsets to be rather minor (<~5%). Lee et al. (2009) documented a similar invigoration process for very thin stratiform

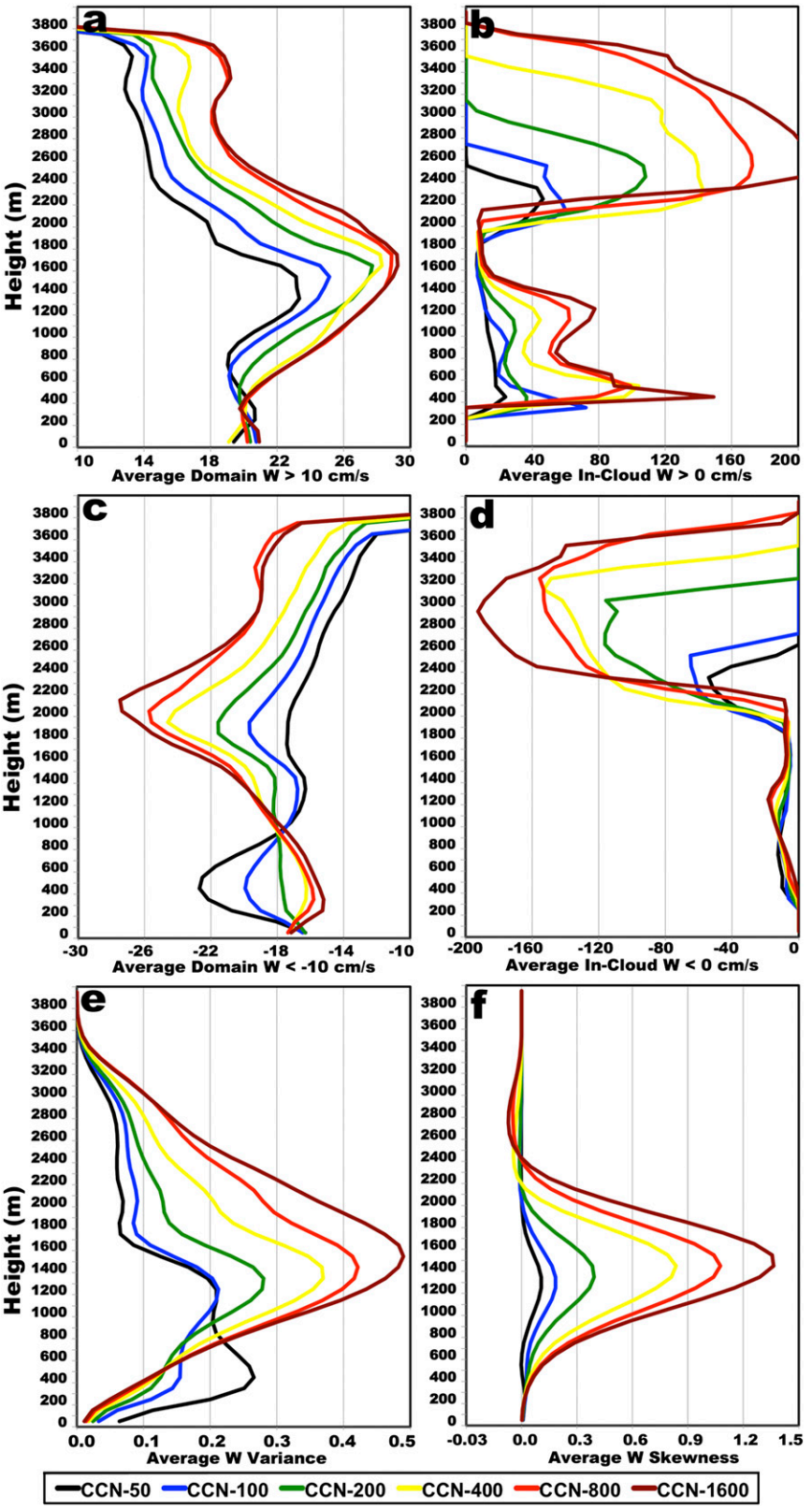


FIG. 9. Temporally and spatially averaged vertical profiles of (a) all updrafts $> 10\,\mathrm{cm\,s^{-1}}$, (b) in-cloud updrafts, (c) downdrafts $< -10\,\mathrm{cm\,s^{-1}}$, (d) in-cloud downdrafts, (e) vertical velocity variance, and (f) vertical velocity skewness. Grid cells were considered in cloud if the cloud mixing ratio exceeded $0.01\,\mathrm{g\,kg^{-1}}$.

clouds. The aerosol-induced condensational invigoration process is likely the primary cause for increased vertical velocity since weaker cold pools (Figs. 8a–d) and reduced surface convergence (Figs. 8e,f) limit the significance of cold-pool outflow interactions as a causal mechanism for increased updraft strength as [CCN] increases.

Mass conservation in this system of clouds requires generation of compensating downdrafts (Jiang and Feingold 2006; Xue and Feingold 2006; Katzwinkel et al. 2014). Above the stratiform cloud base, there is an increase in the compensating downdraft strength with [CCN] (Figs. 9c,d). Below the stratiform cloud base, the downdraft strength weakens with [CCN]. Less evaporative cooling from reduced rain evaporation, discussed above, generates less negatively buoyant air for fueling downdrafts.

The profile of mean vertical velocity variance is displayed in Fig. 9e. The profile from the cleanest simulation is quite comparable to that in Stevens et al. (2001, their Fig. 4d) in both shape and magnitude. The variance profiles reveal an increase with [CCN] above the subcloud layer that peaks in magnitude within the middle of the stratocumulus layer and is indicative of the general increase in both updraft and downdrafts strengths. In contrast, the variance decreases with increased [CCN] in the lower portions of the subcloud layer. The increase in variance aloft points toward increased turbulence and mixing within cloud layers as [CCN] increases. Increased turbulent mixing will tend to entrain greater amounts dry air from above the inversion and lead to cloud erosion. This effect would tend to be maximized in the stratocumulus layer. Further, as discussed previously, a distribution of more numerous, small cloud droplets at high [CCN] will more readily evaporate and accentuate the desiccation of clouds (Zhao and Austin 2005; Lee et al. 2009). Increased turbulence and mixing with an increase in [CCN] will also tend to enhance the deepening of the boundary layer and increase the height of the inversion (Fig. 10). This increase in the inversion height with [CCN] supports the suggestion made in section 3b that the increase in mean cloud-top height with [CCN] results from a deeper boundary layer and greater inversion height. The decrease in vertical velocity variance with [CCN] within the subcloud layer is likely tied to the presence of weaker cold pools and reduced surface convergence. Weaker surface convergence will tend to produce a more uniform vertical velocity field near the surface, whereas stronger cold pools in a low-[CCN] environment would generate a larger inhomogeneity in vertical motion as cold pools collide and impact convergence and forced upward motion.

The skewness of vertical velocity (Fig. 9f) displays a positive monotonic increase with [CCN] over the depth of the primary cloud layer. In general, positive skewness indicates the presence of narrow, strong updrafts and widespread, weak downdrafts (Moeng and Rotunno 1990; Hogan et al. 2009). The increase in positive skewness with [CCN] indicates greater asymmetry in the vertical velocity distribution, which is consistent with the profiles of stronger updrafts and downdrafts at higher [CCN] (Figs. 9a,c). In combination with greater turbulent mixing aloft, the generation of stronger, widespread downdrafts tends to increase the desiccation of the stratocumulus layer as [CCN] increases. In low-LWP clouds, this may mean full cloud erosion. Recent work by Jonker et al. (2008) and Katzwinkel et al. (2014) suggests that stronger vertical motions associated with trade cumuli tend to lead to stronger, localized downdrafts in the vicinity of lateral cloud boundaries. The increase in positive vertical velocity skewness with increasing [CCN] and stronger average downdrafts above the subcloud layer suggests the potential presence of an increase in both 1) widespread, relatively strong downdrafts that could contribute to widespread, gradual stratiform erosion and 2) localized, relatively, strong downdrafts that could lead to more rapid stratiform cloud erosion in the vicinity of towering cumuli.

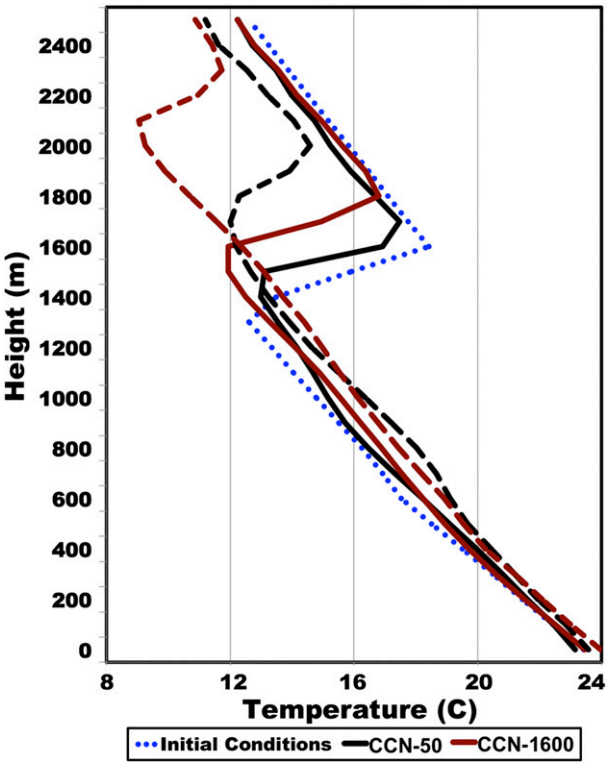


FIG. 10. Vertical profiles of temperature at simulation times 0 (blue dotted, initial conditions), 12 (solid), and 36 h (dashed).

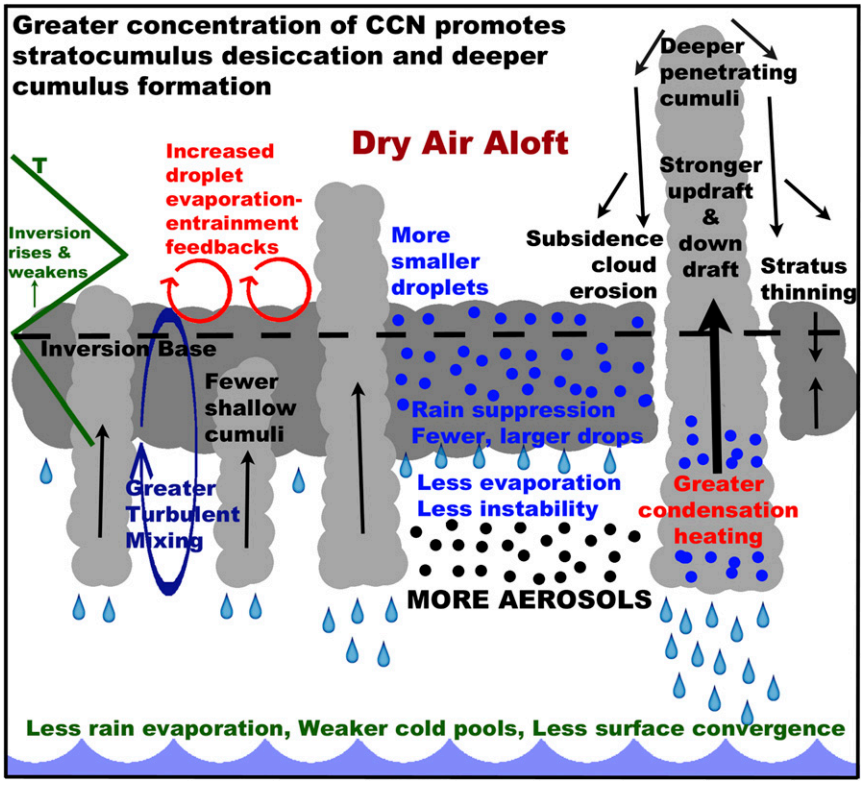


FIG. 11. Schematic highlighting the key changes in cloud microphysical and dynamical processes that occur in response to an increase in CCN aerosols within a warm-phase, multi-regime cloud field.

## 4. Summary and conclusions

In this idealized cloud-modeling study, the RAMS model was used to simulate the effects of aerosols on three distinct warm-phase cloud regimes occurring within the same domain: low-level cumulus, stratocumulus, and deeper cumulus clouds. These warm-phase cloud-resolving simulations were performed in the absence of large-scale forcing in order to explore the range of aerosol effects on cloud microphysical processes and cloud dynamic–thermodynamic feedbacks without artificially damping these processes. As such, the results presented herein likely represent the upper limit of aerosol-induced effects within this environment containing multiple cloud regimes.

Many of the cloud properties shown herein, such as LWP and cloud fraction, and the responses to changes in [CCN] are in agreement with other studies involving a stratocumulus layer topped by a dry inversion (Stevens et al. 1998; Jiang et al. 2002; Jiang and Feingold 2006; Ackerman et al. 2004; Xue et al. 2008; Lee et al. 2009), thus indicating a comparative robustness of our simulations to generate the desired warm-phase clouds. By exploring the upper limit of aerosol-induced changes in the microphysical processes of the warm-phase clouds in this study and the changes in the dynamic and thermodynamic feedbacks, we were able to demonstrate distinct linkages between the microphysical and dynamical processes and their relative influence on the various coexisting and interacting cloud regimes, cloud characteristics, and precipitation. The schematic in Fig. 11 summarizes the aerosol-induced changes in cloud microphysics, dynamics, and thermodynamics that have been presented.

For higher [CCN], there is a noted increase in cloud mixing ratio and number concentration and a decrease in cloud droplet size. There is also an increase in rain mixing ratio but a production of fewer, but larger, raindrops. Microphysical budget analyses revealed a decrease in the collision–coalescence process within the stratocumulus layer that led to less warm-rain production and reduced light precipitation. There was also an increase in the condensation growth of cloud water that promoted an increase in latent heat release and stronger vertical motion. Further, in regions of cloud droplet evaporation, the evaporation rates were greater for higher [CCN]; this process supports greater entrainment–evaporation and latent cooling, which subsequently supports subsidence and cloud erosion.

The vertical velocity variance increased with higher [CCN] above the subcloud layer, suggesting greater turbulence and mixing in the cloud layers, which tend to enhance entrainment of air from above the inversion into the cloud layer. With dry air above the inversion, greater entrainment led to erosion of the stratocumulus layer and lower-LWP clouds. Stronger entrainment–evaporation feedback effects resulting from more efficient cloud droplet evaporation in the more polluted cases likely assisted in the desiccation of the stratocumulus layer. An increase in the vertical velocity skewness with an increase in [CCN] suggested the presence of increasingly strong updrafts and relatively weaker but widespread downdrafts. In addition to more widespread downdrafts, the downdrafts were stronger above the subcloud layer as [CCN] was increased. The increased strength and widespread nature of the subsidence motion also supported erosion of the stratocumulus layer.

In the subcloud layer, the presence of fewer but larger raindrops and overall rainfall suppression for high [CCN] led to a decrease in rain evaporation and reduced latent cooling, which weakened downdraft strength. This produced less negatively buoyant downdrafts near the surface, warmer cold pools, weaker surface convergence, reduced area of cold-pool influence, reduced area of surface convergence, and fewer and weaker near-surface updrafts. These decreases in the strength of cloud thermodynamic–dynamic feedbacks with increasing [CCN] suppressed the forcing for production of the low-level cumuli that feed moisture to help sustain the stratocumulus layer.

The combination and interaction of the microphysical and dynamical processes summarized above resulted in an increase in cloud-base height for greater [CCN] that was attributed to the presence of fewer low-level cumuli under the stratocumulus layer. For increased [CCN] there was also a monotonic decrease in the cloud fraction and depth of the stratocumulus layer due to enhanced cloud erosion effects from greater turbulence and mixing down of dry air, greater widespread downdraft subsidence, and greater entrainment–evaporation effects. Further, the height of the stratocumulus layer increased, likely from deepening of the boundary layer and increased inversion height resulting from increased turbulent mixing. At the same time, there was an increase in the depth and strength of the more isolated deep cumuli that experienced aerosol-invigoration effects from increased condensation and latent heating.

Results from these warm-phase cloud simulations demonstrate aerosol impacts on the responses between multiple coexisting clouds types and the overall cloud scene. The variability in aerosol-induced dynamic and thermodynamic feedbacks related to evaporation–entrainment, vertical motion, and evaporatively generated cold pools led to pronounced differences in predominant cloud type. This was demonstrated by a relative decrease in occurrence of moderate-LWP clouds and a relative increase in the occurrence of both low- and high-LWP clouds for an increase in [CCN]. The loss of the moderate-LWP (moderate rain rates) clouds led to a 50% reduction in the total domain accumulated rainfall volume from the cleanest to most polluted environment, while the increased frequency of deep cumuli led to greater localized rainfall rates. Therefore, increasing [CCN] produces more intense rainfall events that are less frequent in occurrence.

Though not the focus of this study, the aerosol-induced changes in cloud regime have implications for the radiation budget. Reduced cloud fraction in the case of high [CCN] would allow for increases in both incoming shortwave and outgoing longwave radiation. Lower-LWP clouds may or may not impact optical depth and cloud albedo depending on the relative changes in cloud droplet size and the cloud thickness. As such, both the cloud microphysical responses to aerosols and the dynamic and thermodynamic feedbacks to the cloud system affect the cloud regime, precipitation processes, and radiation budgets, all of which are critical to understanding Earth's climate system.

The propensity for deeper clouds with greater precipitation rates aloft at higher [CCN] supports a similar finding from the satellite survey of L'Ecuyer et al. (2009) in which deeper convection was sampled. The aerosol studies cited within this manuscript suggest that cloud LWP can either increase or decrease with [CCN] depending on the environmental conditions, while the satellite study of Lebsock et al. (2008) supports an LWP increase with [CCN] in precipitating clouds. The discrepancies among these studies most likely arise as a result of the sampling of clouds in varying environmental conditions, thus highlighting the impacts of the environment on the variations in the range and sign of aerosol influences on cloud systems.

*Acknowledgments.* This work was supported by the National Aeronautics and Space Administration Division of Atmospheric Science Award NNX12AC51G.

## REFERENCES

Ackerman, A. S., M. P. Kirkpatrick, D. E. Stevens, and O. B. Toon, 2004: The impact of humidity above stratiform clouds on indirect aerosol climate forcing. *Nature,* **432,** 1014–1017, doi:10.1038/nature03174.

Albrecht, B. A., 1979: A model of the thermodynamic structure of the trade-wind boundary layer: Part II. Applications. *J. Atmos. Sci.,* **36,** 90–98, doi:10.1175/1520-0469(1979)036<0090:AMOTTS>2.0.CO;2.

——, 1989: Aerosols, cloud microphysics, and fractional cloudiness. *Science,* **245,** 1227–1230, doi:10.1126/science.245.4923.1227.

Altaratz, O., I. Koren, T. Reisin, A. Kostinski, G. Feingold, Z. Levin, and Y. Yin, 2008: Aerosols' influence on the interplay between condensation, evaporation and rain in warm cumulus cloud. *Atmos. Chem. Phys.,* **8,** 15–24, doi:10.5194/acp-8-15-2008.

Augstein, E., H. Riehl, F. Ostapoff, and V. Wagner, 1973: Mass and energy transports in an undisturbed Atlantic trade-wind flow. *Mon. Wea. Rev.,* **101,** 101–111, doi:10.1175/1520-0493(1973)101<0101:MAETIA>2.3.CO;2.

——, H. Schmidt, and F. Ostapoff, 1974: The vertical structure of the atmospheric planetary boundary layer in undisturbed trade winds over the Atlantic Ocean. *Bound.-Layer Meteor.,* **6,** 129–150, doi:10.1007/BF00232480.

Berg, W., T. L'Ecuyer, and C. Kummerow, 2006: Rainfall climate regimes: The relationship of regional TRMM rainfall biases to the environment. *J. Appl. Meteor. Climatol,* **45,** 434–454, doi:10.1175/JAM2331.1.

——, ——, and S. C. van den Heever, 2008: Evidence for the impact of aerosols on the onset and microphysical properties of rainfall from a combination of satellite observations and cloud-resolving model simulations. *J. Geophys. Res.,* **113,** D14S23, doi:10.1029/2007JD009649.

Blyth, A. M., W. A. Cooper, and J. B. Jensen, 1988: A study of the source of entrained air in Montana cumuli. *J. Atmos. Sci.,* **45,** 3944–3964, doi:10.1175/1520-0469(1988)045<3944:ASOTSO>2.0.CO;2.

Brümmer, B., E. Augstein, and H. Riehl, 1974: On the low-level wind structure in the Atlantic trade. *Quart. J. Roy. Meteor. Soc.,* **100,** 109–121, doi:10.1002/qj.49710042310.

Cheng, W. Y. Y., G. G. Carrio, W. R. Cotton, and S. M. Saleeby, 2009: Influence of atmospheric aerosols on the development of precipitating trade wind cumuli in a large eddy simulation. *J. Geophys. Res.,* **114,** D08201, doi:10.1029/2008JD011011.

Cotton, W. R., and Coauthors, 2003: RAMS 2001: Current status and future directions. *Meteor. Atmos. Phys.,* **82,** 5–29, doi:10.1007/s00703-001-0584-9.

Feingold, G., W. R. Cotton, B. Stevens, and A. S. Frisch, 1996: The relationship between drop in-cloud residence time and drizzle production in numerically simulated stratocumulus clouds. *J. Atmos. Sci.,* **53,** 1108–1122, doi:10.1175/1520-0469(1996)053<1108:TRBDIC>2.0.CO;2.

——, R. L. Walko, B. Stevens, and W. R. Cotton, 1998: Simulations of marine stratocumulus using a new microphysical parameterization scheme. *Atmos. Res.,* **47–48,** 505–528, doi:10.1016/S0169-8095(98)00058-1.

Hahn, C. J., and S. G. Warren, 2007: A gridded climatology of clouds over land (1971–96) and ocean (1954–97) from surface observations worldwide. Numeric Data Package NDP-026E ORNL/CDIAC-153, CDIAC, Department of Energy, 71 pp, doi:10.3334/CDIAC/cli.ndp026e.

Harrington, J. Y., 1997: The effects of radiative and microphysical processes on simulated warm and transition season Arctic stratus. Ph.D. dissertation, Colorado State University, Atmospheric Science Paper 637, 289 pp. [Available online at http://www.meteo.psu.edu/~jyh10/pubs/dis.pdf.]

Hartmann, D. L., M. E. Ockert-Bell, and M. L. Michelsen, 1992: The effect of cloud type on earth's energy balance—Global analysis. *J. Climate,* **5,** 1281–1304, doi:10.1175/1520-0442(1992)005<1281:TEOCTO>2.0.CO;2.

Hogan, R. J., A. L. M. Grant, A. J. Illingsworth, G. N. Pearson, and E. J. O'Connor, 2009: Vertical velocity variance and skewness in clear and cloud-topped boundary layers as revealed by Doppler lidar. *Quart. J. Roy. Meteor. Soc.,* **135,** 635–643, doi:10.1002/qj.413.

Jiang, H., and G. Feingold, 2006: Effect of aerosol on warm convective clouds: Aerosol-cloud-surface flux feedbacks in a new coupled large eddy model. *J. Geophys. Res.,* **111,** D01202, doi:10.1029/2005JD006138.

——, ——, and W. R. Cotton, 2002: Simulations of aerosol-cloud-dynamical feedbacks resulting from entrainment of aerosol into the marine boundary layer during the Atlantic Stratocumulus Transition Experiment. *J. Geophys. Res.,* **107,** 4813, doi:10.1029/2001JD001502.

Jonker, H. J. J., T. Heus, and P. P. Sullivan, 2008: A refined view of vertical mass transport by cumulus convection. *Geophys. Res. Lett.,* **35,** L07810, doi:10.1029/2007GL032606.

Katzwinkel, J., H. Siebert, T. Heus, and R. A. Shaw, 2014: Measurements of turbulent mixing and subsiding shells in trade wind cumuli. *J. Atmos. Sci.,* **71,** 2810–2822, doi:10.1175/JAS-D-13-0222.1.

Kaufman, Y. J., I. Koren, L. A. Remer, D. Rosenfeld, and Y. Rudich, 2005: The effect of smoke, dust and pollution aerosol on shallow cloud development over the Atlantic Ocean. *Proc. Natl. Acad. Sci. USA,* **102,** 11 207–11 212, doi:10.1073/pnas.0505191102.

Khain, A. P., N. BenMoshe, and A. Pokrovsky, 2008: Factors determining the impact of aerosols on surface precipitation from clouds: An attempt at classification. *J. Atmos. Sci.,* **65,** 1721–1748, doi:10.1175/2007JAS2515.1.

Koren, I., Y. J. Kaufman, D. Rosenfeld, L. A. Remer, and Y. Rudich, 2005: Aerosol invigoration and restructuring of Atlantic convective clouds. *Geophys. Res. Lett.,* **32,** L14828, doi:10.1029/2005GL023187.

Lebsock, M. D., G. L. Stephens, and C. Kummerow, 2008: Multisensor satellite observations of aerosol effects on warm clouds. *J. Geophys. Res.,* **113,** D15205, doi:10.1029/2008JD009876.

L'Ecuyer, T. S., W. Berg, J. Haynes, M. Lebsock, and T. Takemura, 2009: Global observations of aerosol impacts on precipitation occurrence in warm maritime clouds. *J. Geophys. Res.,* **114,** D09211, doi:10.1029/2008JD011273.

Lee, S. S., J. E. Penner, and S. M. Saleeby, 2009: Aerosol effects on liquid-water path of thin stratocumulus clouds. *J. Geophys. Res.,* **114,** D07204, doi:10.1029/2008JD010513.

Matsui, T., H. Masunaga, R. A. Pielki Sr., and W.-K. Tao, 2004: Impact of aerosols and atmospheric thermodynamics on cloud properties within the climate system. *Geophys. Res. Lett.,* **31,** L06109, doi:10.1029/2003GL019287.

Meyers, M. P., R. L. Walko, J. Y. Harrington, and W. R. Cotton, 1997: New RAMS cloud microphysics parameterization. Part II. The two-moment scheme. *Atmos. Res.,* **45,** 3–39, doi:10.1016/S0169-8095(97)00018-5.

Moeng, C. H., and R. Rotunno, 1990: Vertical-velocity skewness in the buoyancy-driven boundary layer. *J. Atmos. Sci.,* **47,** 1149–1162, doi:10.1175/1520-0469(1990)047<1149:VVSITB>2.0.CO;2.

Paluch, I. R., and D. H. Lenschow, 1991: Stratiform cloud formation in the marine boundary layer. *J. Atmos. Sci.,* **48,** 2141–2158, doi:10.1175/1520-0469(1991)048<2141:SCFITM>2.0.CO;2.

Riehl, H., and J. S. Malkus, 1957: On the heat balance and maintenance of the circulation in the trades. *Quart. J. Roy. Meteor. Soc.,* **83,** 21–29, doi:10.1002/qj.49708335503.

Rossow, W. B., and R. A. Schiffer, 1999: Advances in understanding clouds from ISCCP. *Bull. Amer. Meteor. Soc.,* **80,** 2261–2287, doi:10.1175/1520-0477(1999)080<2261:AIUCFI>2.0.CO;2.

Saleeby, S. M., and W. R. Cotton, 2004: A large droplet mode and prognostic number concentration of cloud droplets in the Colorado State University Regional Atmospheric Modeling

System (RAMS). Part I: Module descriptions and supercell test simulations. *J. Appl. Meteor.,* **43,** 182–195, doi:10.1175/1520-0450(2004)043<0182:ALMAPN>2.0.CO;2.

——, and S. C. van den Heever, 2013: Developments in the CSU-RAMS aerosol model: Emissions, nucleation, regeneration, deposition, and radiation. *J. Appl. Meteor. Climatol.,* **52,** 2601–2622, doi:10.1175/JAMC-D-12-0312.1.

——, W. Berg, T. L'Ecuyer, and S. C. van den Heever, 2010: Impact of cloud-nucleating aerosols in cloud-resolving model simulations of warm-rain precipitation in the East China Sea. *J. Atmos. Sci.,* **67,** 3916–3930, doi:10.1175/2010JAS3528.1.

Sassen, K., and Z. Wang, 2008: Classifying clouds around the globe with the CloudSat radar: 1-year of results. *Geophys. Res. Lett.,* **35,** L04805, doi:10.1029/2007GL032591.

Savic-Jovcic, V., and B. Stevens, 2008: The structure and mesoscale organization of precipitating stratocumulus. *J. Atmos. Sci.,* **65,** 1587–1605, doi:10.1175/2007JAS2456.1.

Seifert, A., and K. D. Beheng, 2006: A two-moment cloud microphysics parameterization for mixed-phase clouds. Part 2: Maritime vs. continental deep convective storms. *Meteor. Atmos. Phys.,* **92,** 67–82, doi:10.1007/s00703-005-0113-3.

Sekiguchi, M., T. Nakajima, K. Suzuki, K. Kawamoto, A. Higurashi, D. Rosenfeld, I. Sano, and S. Mukai, 2003: A study of the direct and indirect effects of aerosols using global satellite data sets of aerosol and cloud parameters. *J. Geophys. Res.,* **108,** 4699, doi:10.1029/2002JD003359.

Smagorinsky, J., 1963: General circulation experiments with the primitive equations. *Mon. Wea. Rev.,* **91,** 99–164, doi:10.1175/1520-0493(1963)091<0099:GCEWTP>2.3.CO;2.

Solomon, S., and Coauthors, 2007: Technical summary. *Climate Change 2007: The Physical Science Basis,* S. Solomon et al., Eds., Cambridge University Press, 19–91.

Stevens, B., W. R. Cotton, G. Feingold, and C.-H. Moeng, 1998: Large-eddy simulations of strongly precipitating, shallow, stratocumulus-topped boundary layers. *J. Atmos. Sci.,* **55,** 3616–3638, doi:10.1175/1520-0469(1998)055<3616:LESOSP>2.0.CO;2.

——, and Coauthors, 2001: Simulations of trade wind cumuli under a strong inversion. *J. Atmos. Sci.,* **58,** 1870–1891, doi:10.1175/1520-0469(2001)058<1870:SOTWCU>2.0.CO;2.

Storer, R. L., and S. C. van den Heever, 2013: Microphysical processes evident in aerosol forcing of tropical deep convective clouds. *J. Atmos. Sci.,* **70,** 430–446, doi:10.1175/JAS-D-12-076.1.

——, ——, and G. L. Stephens, 2010: Modeling aerosol impacts on convective storms in different environments. *J. Atmos. Sci.,* **67,** 3904–3915, doi:10.1175/2010JAS3363.1.

Turner, D. D., and Coauthors, 2007: Thin liquid water clouds: Their importance and their challenge. *Bull. Amer. Meteor. Soc.,* **88,** 177–190, doi:10.1175/BAMS-88-2-177.

Twomey, S., 1974: Pollution and the planetary albedo. *Atmos. Environ.,* **8,** 1251–1256, doi:10.1016/0004-6981(74)90004-3.

——, 1977: The influence of pollution on the shortwave albedo of clouds. *J. Atmos. Sci.,* **34,** 1149–1152, doi:10.1175/1520-0469(1977)034<1149:TIOPOT>2.0.CO;2.

Tzivion (Tzitzvashvili), S., G. Feingold, and Z. Levin, 1987: An efficient numerical solution to the stochastic collection equation. *J. Atmos. Sci.,* **44,** 3139–3149, doi:10.1175/1520-0469(1987)044<3139:AENSTT>2.0.CO;2.

van den Heever, S. C., G. L. Stephens, and N. B. Wood, 2011: Aerosol indirect effects on tropical convection characteristics under conditions of radiative–convective equilibrium. *J. Atmos. Sci.,* **68,** 699–718, doi:10.1175/2010JAS3603.1.

Waite, M. L., and B. Khouider, 2010: The deepening of tropical convection by congestus preconditioning. *J. Atmos. Sci.,* **67,** 2601–2615, doi:10.1175/2010JAS3357.1.

Walko, R. L., W. R. Cotton, M. P. Meyers, and J. Y. Harrington, 2000a: Efficient computation of vapor and heat diffusion between hydrometeors in a numerical model. *Atmos. Res.,* **53,** 171–183, doi:10.1016/S0169-8095(99)00044-7.

——, and Coauthors, 2000b: Coupled atmosphere–biophysics–hydrology models for environmental modeling. *J. Appl. Meteor.,* **39,** 931–944, doi:10.1175/1520-0450(2000)039<0931:CABHMF>2.0.CO;2.

Wood, R., 2012: Review: Stratocumulus clouds. *Mon. Wea. Rev.,* **140,** 2373–2423, doi:10.1175/MWR-D-11-00121.1.

Xue, H., and G. Feingold, 2006: Large-eddy simulations of trade wind cumuli: Investigation of aerosol indirect effects. *J. Atmos. Sci.,* **63,** 1605–1622, doi:10.1175/JAS3706.1.

——, ——, and B. Stevens, 2008: Aerosol effects on clouds, precipitation, and the organization of shallow cumulus convection. *J. Atmos. Sci.,* **65,** 392–406, doi:10.1175/2007JAS2428.1.

Zhao, M., and P. H. Austin, 2005: Life cycle of numerically simulated shallow cumulus clouds. Part I: Transport. *J. Atmos. Sci.,* **62,** 1269–1290, doi:10.1175/JAS3414.1.